Energy &
Environmental
Science

ROYAL SOCIETY
OF CHEMISTRY

COMMUNICATION

View Article Online
View Journal

Check for updates

Cite this: DOI: 10.1039/c9ee03219c

Received 7th October 2019,
Accepted 21st January 2020

DOI: 10.1039/c9ee03219c

rsc.li/ees

Ionogel-based sodium ion micro-batteries with a 3D Na-ion diffusion mechanism enable ultrahigh rate capability†

Shuanghao Zheng,[abc] Huijuan Huang,[d] Yanfeng Dong,[a] Sen Wang,[ac] Feng Zhou,[a] Jieqiong Qin,[ac] Chenglin Sun,[a] Yan Yu,*[de] Zhong-Shuai Wu*[a] and Xinhe Bao[ab]

The rapid development of microelectronics and microsystems has stimulated the continuous evolution of high-performance and cost-effective micro-batteries. Despite their competitiveness with huge application potential, sodium ion micro-batteries (NIMBs) are still underdeveloped. Herein, we demonstrate one prototype of a quasi-solid-state planar ionogel-based NIMB constructed by separator-free interdigital microelectrodes of sodium titanate anode and sodium vanadate phosphate cathode, both of which are embedded into a three-dimensional interconnected graphene scaffold. Meanwhile, a novel $NaBF_4$-based ionogel electrolyte with robust ionic conductivity of 8.1 mS cm^{-1} was used. Benefiting from the synergetic merits from the planar architecture, dominant pseudo-capacitance contribution, and 3D multi-directional Na-ion diffusion mechanism, the as-assembled NIMBs exhibit high volumetric capacity of 30.7 mA h cm^{-3} at 1C, and high rate performance with 15.7 mA h cm^{-3} at 30C at room temperature and 13.5 mA h cm^{-3} at 100C at a high temperature of 100 °C. Moreover, the quasi-solid-state NIMBs present outstanding flexibility, tunable voltage and capacity output, and remarkable areal energy density of 145 μW h cm^{-2} (55.6 mW h cm^{-3}). Therefore, this work will provide numerous chances to construct planar NIMBs for microsystems.

Broader context

With the upcoming booming popularity of flexible and wearable microelectronics, the Internet of Things, and self-powered microsystems, it is urgently required to explore new-concept advanced microelectrochemical energy storage devices with high-performance and various form factors beyond currently available stacked micro-battery technologies. Among the key strategies to realize this purpose, planar micropower sources, free of separator, have recently garnered extensive attention as a highly competitive system, with exceptional capability of form factor-free, design diversity, and outstanding shape/performance compatibility with various microelectronics, allowing for seamless integration in particular with complex-shaped electronics. Planar sodium ion micro-batteries (NIMBs) are considered as a new class of promising micropower sources, but remain challenging. Herein, we constructed flexible nonaqueous planar NIMBs based on a sodium titanate anode and sodium vanadate phosphate cathode, both of which are encapsulated into a 3D conductive graphene network, using a novel $NaBF_4$-based ionogel electrolyte with high ionic conductivity of 8.1 mS cm^{-1}. The resulting NIMBs show remarkable areal energy density, robust rate capability, outstanding flexibility, and tunable voltage and capacity output, owing to the effective coupling effect with an advanced planar geometry, multi-directional Na-ion diffusion pathways, and pseudocapacitive contribution. Moreover, it is proposed that planar microscale energy storage devices are an ideal *in situ* characterization model for the charge storage mechanism.

Introduction

High-performance, flexible and integrated micro-batteries with sufficient energy and form factors are urgently needed to satisfy the rapid and continuous development of microelectronics and microsystems,[1–7] including wireless sensors, implantable medical devices, radio frequency identification, and portable or wearable electronics.[8–11] Lithium ion micro-batteries (LIMBs) with high energy density are currently the most popular micro-scale power sources.[12–16] In particular, planar LIMBs with interdigital microelectrodes have been extensively investigated. The ion diffusion pathway is effectively shortened and no separator is required in such an architecture, which enlarges

---

[a] *Dalian National Laboratory for Clean Energy, Dalian Institute of Chemical Physics, Chinese Academy of Sciences, 457 Zhongshan Road, Dalian 116023, China. E-mail: wuzs@dicp.ac.cn*
[b] *State Key Laboratory of Catalysis, Dalian Institute of Chemical Physics, Chinese Academy of Sciences, 457 Zhongshan Road, Dalian 116023, China*
[c] *University of Chinese Academy of Sciences, 19 A Yuquan Rd, Shijingshan District, Beijing, 100049, China*
[d] *Hefei National Laboratory for Physical Sciences at the Microscale, Department of Materials Science and Engineering, CAS Key Laboratory of Materials for Energy Conversion, University of Science and Technology of China, Hefei, Anhui, 230026, China. E-mail: yanyumse@ustc.edu.cn*
[e] *State Key Laboratory of Fire Science, University of Science and Technology of China, Hefei, Anhui, 230026, China*

† Electronic supplementary information (ESI) available: TEM and XRD of NTO, TEM and XRD of NVP, TEM of EG, EIS spectra, electrical conductivity, flexibility and high-temperature performance. See DOI: 10.1039/c9ee03219c

the fraction of electroactive material and increases the energy density of the micro-battery system. Besides, they can be seamlessly integrated into microelectronic devices mounted on a planar integrated circuit, facilitating the miniaturization of the entire microelectronic system.[13,17,18] However, development of LIMBs is limited by the scarcity, uneven distribution and increasing cost of metal lithium.[13,19,20]

To address the above issues, extensive efforts have been dedicated to the exploitation of sodium ion micro-batteries (NIMBs), because sodium is naturally abundant, low cost, and shows a similarly low potential (−2.7 V *vs.* SHE) to lithium.[21–25] Moreover, sodium ions with larger size are inclined to form weakly solvated ion clusters in aprotic solvent, making them more conductive than lithium ions and it is thus more feasible to achieve high-power NIMBs.[26–28] So far, several electrode materials, such as $Na_2Ti_3O_7$ nanoarrays,[29,30] Sb nanorod arrays,[31] Cu_3P nanowires,[32] SnS nanoarrays[33] and vertically aligned $MoSe_2$ arrays,[34] have been demonstrated for NIMBs with a conventional stacked geometry. However, reasonable construction of planar NIMBs with high performance and form factors is rarely reported due to the challenges of lacking an effective electron–ion diffusion network and suitable electrolyte.

Herein, we first constructed quasi-solid-state flexible non-aqueous planar interdigital NIMBs based on an urchin-like sodium titanate (NTO) anode and flower-like sodium vanadate phosphate (NVP) cathode with super ionic conductivity, both of which were encapsulated into a 3D highly conductive network composed of graphene nanosheets. As a result, the as-fabricated anode and cathode microelectrodes with a metal-free current collector exhibited high electrical conductivity of 160 and 180 S cm^{-1}, respectively. The novel $NaBF_4$-based ionogel electrolyte possessed high ionic conductivity of 8.1 mS cm^{-1}, comparable to an aqueous gel electrolyte. The quasi-solid-state NIMBs showed high volumetric capacity of 30.7 mA h cm^{-3} at 1C and robust rate capability with 15.7 mA h cm^{-3} at 30C under an ambient environment and 13.5 mA h cm^{-3} at 100C at 100 °C, owing to effectively coupling with the planar geometry, dominant multi-directional sodium ion diffusion pathways, and pseudocapacitive contribution. Moreover, the as-assembled NIMBs displayed not only an ultrahigh areal energy density of 145 μW h cm^{-2}, but also exceptional flexibility and seamless modular integration with tunable voltage and current output.

Results and discussion

The configuration of NIMBs is systematically elucidated in Fig. 1a–c. Initially, high electrical conducting exfoliated graphene (EG, 1000 S cm^{-1}, Fig. 1a and Fig. S1, ESI†) nanosheets were prepared by an electrochemical method,[35,36] and directly filtrated on nylon membrane to establish an interdigitated metal-free current collector. Additionally, EG nanosheets were utilized as both a 2D conductive additive and flexible support to form conductive microelectrodes. Subsequently, a NTO anode with advantages of high capacity, a stable structure with a slight volume change during the charge/discharge process and low potential of Na^+ ion insertion (<0.5 *vs.* Na^+/Na),[22,37,38] was directly deposited on one side of the interdigital EG micro-patterns (Fig. 1b). Meanwhile, the NVP cathode possessing a high and flat operating voltage plateau, exceptional structural stability and intrinsic high ionic diffusivity,[39–41] was placed on the other side to form the asymmetric in-plane microelectrodes (Fig. 1c). It is worth mentioning that the NTO, synthesized from $Ti_3C_2T_x$ by simultaneous oxidation and alkalization, exhibited urchin-like morphology of intertwined nanoribbons, and a large interlayer spacing of 0.9 nm allowing for rapid insertion and extraction of Na^+ ions (Fig. 1d and Fig. S2, ESI†). And the flower-like microsized NVP prepared by thermal annealing displayed high crystallinity and ultrathin carbon-coating (Fig. 1e and Fig. S3, ESI†), good for improving electron transfer. The as-fabricated microelectrodes exhibited a layer-stacked structure, in which an active material electrode was sandwiched between the bottom and top EG layers. Moreover, large-lateral-size EG nanosheets were thoroughly interpenetrated into the NTO anode or NVP cathode, and well connectedly confined by the bottom and top EG layers, forming a 3D highly conductive EG network (Fig. S4, ESI†). With a reasonable optimization, the as-fabricated microelectrodes showed a typical thickness of ∼5 μm (Fig. 1f and g), and displayed high electronic conductivity of 160 S cm^{-1} for the anode and 180 S cm^{-1} for the cathode (Fig. S5, ESI†). Meanwhile, the interdigital microelectrodes displayed outstanding flexibility without any structure fracture, electrical conductivity change or delamination from the substrate even after repeated severe bending (Fig. 1h, i and Fig. S6, S7, ESI†), indicating its exceptional structural stability. Furthermore, the serially-connected NIMBs also exhibited remarkable resistance to mechanical deformation without any fragmentation or damage (Fig. 1j–l). After an ionogel electrolyte was coated on the microelectrode fingers and solidified, quasi-solid-state NIMBs were finally achieved.

To build quasi-solid-state high-performance and flexible NIMBs, we developed two kinds of sodium ion based ionogel electrolytes with different anions. One is a $NaBF_4$ based ionogel electrolyte (denoted as $NaBF_4$-IE), composed of $NaBF_4$, 1-ethyl-3-methylimidazolium tetrafluoroborate ($EMIMBF_4$) and poly-(vinylidenedifluoride-*co*-hexafluoropropylene) (PVDF-HFP) ($NaBF_4$/$EMIMBF_4$/PVDF-HFP), and the other is a bis(trifluoromethylsulfonyl) imide sodium salt (NaTFSI) based ionogel electrolyte (denoted as NaTFSI-IE), mixed with NaTFSI, 1-ethyl-3-methylimidazolium bis(trifluoromethylsulfonyl) imide (EMIMTFSI) and PVDF-HFP (NaTFSI/EMIMTFSI/PVDF-HFP) (see details in Methods). Remarkably, the ionic conductivity of $NaBF_4$-IE was as high as 8.1 mS cm^{-1} at room temperature (25 °C), which was higher than that of NaTFSI-IE (4.4 mS cm^{-1}, Fig. 2a) and most reported ionogel electrolytes, *e.g.*, bis(fluorosylsulfonyl) imide sodium salt (NaFSI)/*N*-propyl-*N*-methyl pyrrolidine bis(fluorossulfonyl) imide ($P_{13}FSI$) (3.2 mS cm^{-1}).[42] When the temperature increased, the ionic conductivities of $NaBF_4$-IE and NaTFSI-IE also apparently increased, *e.g.*, showing the values of 25 and 11 mS cm^{-1} at 100 °C, respectively. To clarify the disparity between BF_4^- and $TFSI^-$ anions, the Na^+ ion migration number was calculated from the plot of current *vs.* time and the

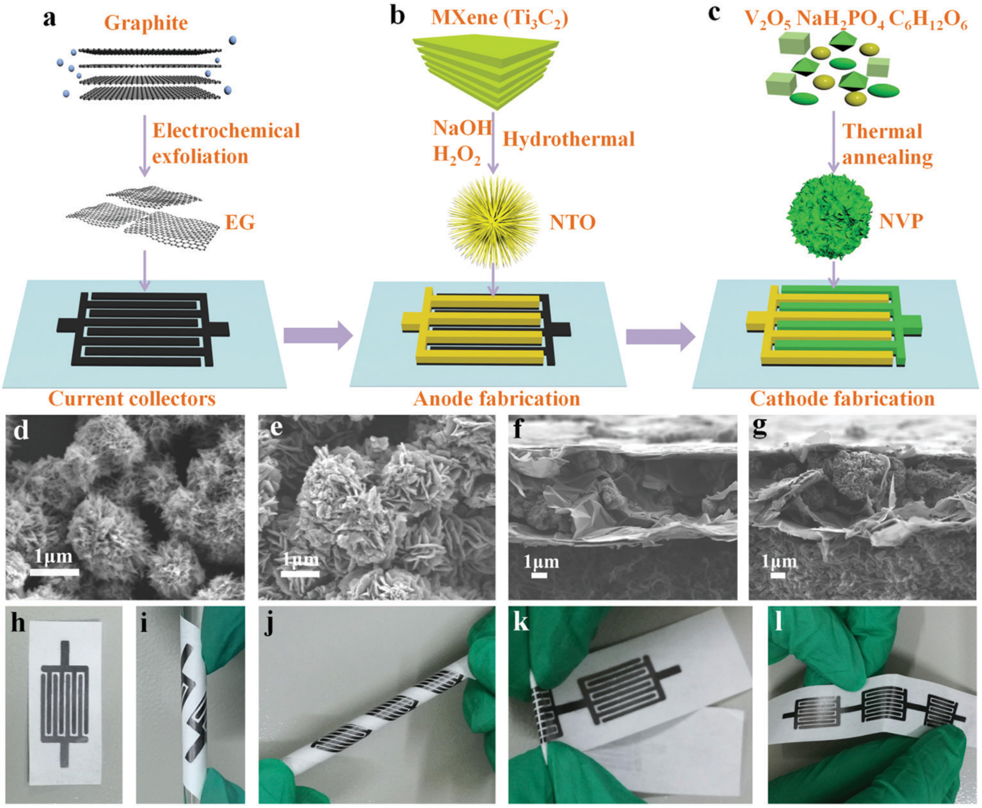

Fig. 1 Construction and characterization of planar NIMBs with an interdigital pattern. (a) Schematic showing the preparation of highly conductive EG as a metal-free current collector. (b) Schematic showing the synthesis of NTO and fabrication of NTO anode. (c) Schematic showing the preparation of NVP and fabrication of the NVP cathode. (d and e) SEM images of NTO (d) and NVP (e). (f and g) Cross-section SEM images of the anode (f) and cathode (g). (h and i) Optical images of an individual NIMB in the flat (h) and twisted (i) states. (j–l) Optical images of three serially-connected NIMBs in the twisted (j), folded (k) and released (l) states.

impedance spectra.[43] Obviously, $NaBF_4$-IE disclosed a larger Na^+ ion migration number of 0.49 than that of NaTFSI-IE (0.25, Fig. 2b and Fig. S8, S9, ESI†), owing to the smaller sodium cluster ion in $NaBF_4$-IE for promoting fast movement in comparison with that in NaTFSI-IE.[44–46] Moreover, the Debye curve, the imaginary impedance as a function of frequency, is related to the relaxation time of ion hopping. The highest frequency at the Debye curve is the characteristic frequency of conductivity relaxation.[47] From Fig. 2c, it was observed that the characteristic frequency was 218 Hz for $NaBF_4$-IE, but only 100 Hz for NaTFSI-IE, further indicating that $NaBF_4$-IE possessed higher ionic conductivity.

To further elucidate this disparity, we investigated the electrochemical performance of quasi-solid-state NIMBs with a thin electrode thickness of 5 μm using $NaBF_4$-IE and NaTFSI-IE, which were marked as NTO|$NaBF_4$-IE|NVP and NTO|NaTFSI-IE|NVP, respectively. As shown in Fig. 2d and Fig. S10 (ESI†), the optimized NTO|$NaBF_4$-IE|NVP presented slope operating charge and discharge voltage profiles between 1.2 and 2.4 V and high specific volumetric capacity of 30.7 mA h cm^{-3} at 1C (100 mA g^{-1}), calculated based on the whole volume of the electrodes, interspace and ionogel electrolyte. While the working voltage of NTO|NaTFSI-IE|NVP was in the range of 1.7–2.6 V (Fig. 2e) and the volumetric capacity at 1C was 15.1 mA h cm^{-3} (about 49% of NTO|$NaBF_4$-IE|NVP), implying that anions complexed with Na^+ ion have a great influence on the performance of NIMBs. The higher capacity of NTO|$NaBF_4$-IE|NVP should originate from the higher ionic conductivity and larger transference number of Na^+ ions in $NaBF_4$-IE. Even at a high current density of 30C within a short discharge time of around 1 min, NTO|$NaBF_4$-IE|NVP still achieved a high volumetric capacity of 15.7 mA h cm^{-3} (Fig. 2f), which was 51% of the initial specific capacity and almost two times higher than that of NTO|NaTFSI-IE|NVP (6.6 mA h cm^{-3}). Accordingly, NTO|$NaBF_4$-IE|NVP delivered an areal capacity of 20 μA h cm^{-2} at 1C, evaluated from the footprint area. With increasing the electrode thickness to 25 μm (denoted as NTO(25)|$NaBF_4$-IE|NVP(25)), the areal capacity of NTO(25)|$NaBF_4$-IE|NVP(25) was substantially magnified to 81 μA h cm^{-2} (Fig. S11, ESI†). After 100 cycles at 1C, NTO(25)|$NaBF_4$-IE|NVP(25) showed dramatically enhanced cyclability with high capacity retention of 75% (Fig. S12, ESI†). Remarkably, NTO|$NaBF_4$-IE|NVP exhibited long-term cycling stability, and maintained a high volumetric capacity of 10.1 mA h cm^{-3} after 3000 cycles at a high rate of 20C (Fig. 2g), corresponding to an average attenuation of only 0.01% per cycle. Note that the capacity contribution of the EG current collectors to the total cell capacity was negligible (0.09%, Fig. S13, ESI†). Because of its superiority, subsequent studies on NIMBs were carried out in $NaBF_4$-IE.

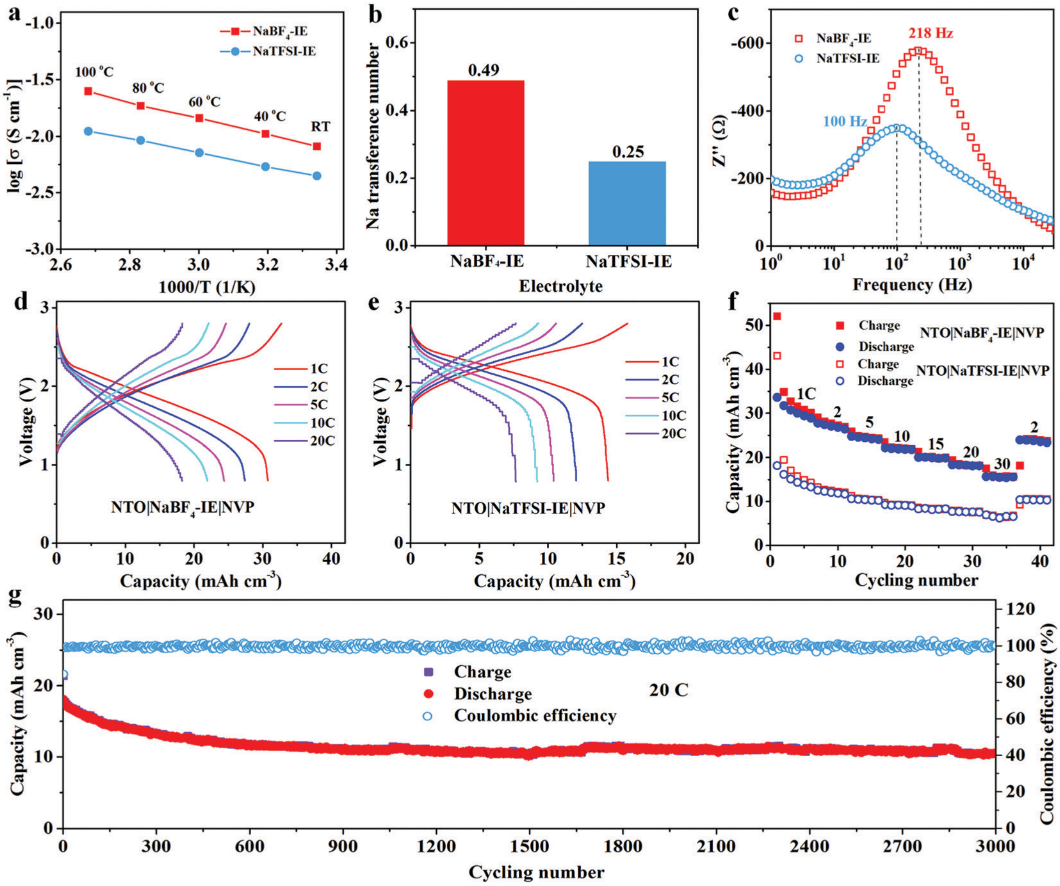

Fig. 2 Electrochemical properties of ionogel electrolyte and electrochemical performance of NIMBs. (a–c) Ionic conductivity (a), Na^+ ion transference number (b) and Debye plots (c) of $NaBF_4$-IE and NaTFSI-IE. (d and e) GCD profiles of NTO|$NaBF_4$-IE|NVP (d) and NTO|NaTFSI-IE|NVP (e). (f) Rate performance of NTO|$NaBF_4$-IE|NVP and NTO|NaTFSI-IE|NVP. (g) Long-term cycling performance of NTO|$NaBF_4$-IE|NVP.

2For a better understanding of the excellent rate performance, Na^+ ion kinetics in NTO|$NaBF_4$-IE|NVP were analyzed by cyclic voltammetry (CV), to distinguish the contribution from capacitive and diffusion-controlled behaviors. As shown in Fig. 3a, CV curves measured from 1 to 10 mV s^{-1} displayed a clear redox couple between 2 and 2.5 V. The anodic and cathodic currents at a certain scan rate obey a power-law relationship: $i = av^b$, where a and b are adjustable constants, i is current and v is scan rate.[48,49] Specifically, a b value of 0.5 indicates a diffusion-controlled faradaic reaction, and $b = 1$ implies a surface-controlled pseudocapacitive reaction. From log(i) *vs.* log(v) plots (Fig. 3b), the b value was calculated to be 0.85, suggestive of the dominant surface-controlled pseudocapacitance contribution. Furthermore, the separate capacitive (k_1v) and diffusion-controlled ($k_2v^{0.5}$) contribution were quantitatively analyzed using the following eqn (1):

$$i = k_1v + k_2v^{0.5} \qquad (1)$$

where k_1 and k_2 are variable constants. By plotting the $v^{0.5}$ *vs.* $i/v^{0.5}$, the values of k_1 and k_2 were determined at a fixed scan rate and voltage from the slope and intercept of the fitted lines.[49] From the analysis, it was found that the capacitive current increased with the scan rate and a dominating capacitive contribution of larger than 60% was achieved (Fig. 3c). For instance, at 8 mV s^{-1}, the capacitive contribution was as high as 80.7% (Fig. 3d), indicative of fast kinetics in NTO|$NaBF_4$-IE|NVP.

The structural evolution of the NTO anode and NVP cathode during a Na-ion insertion/extraction process were elucidated from *in situ* Raman spectra (Fig. 3e, f and Fig. S14, ESI†) and *ex situ* X-ray diffraction (XRD) patterns (Fig. S15, ESI†). Before charging, the main peaks of the NTO anode at 282 and 295 cm^{-1} were ascribed to the Na–O–Ti stretching vibration and the broad peak at 450 cm^{-1} was assigned to Ti–O–Ti vibration.[50–52] While no peaks were observed in the NVP cathode. During the charging process, the intensity of the peak at 282 cm^{-1} decreased and the peak at 295 cm^{-1} gradually disappeared, indicative of the sodiation process of NTO anode. Correspondingly, the characteristic peaks of NVP at 293, 331 and 436 cm^{-1} from the PO_4 and external lattice vibrations appeared[53] and their intensities suddenly increased, owing to the reduction in electrical conductivity of NVP resulting from the formation of the $Na_1V_2(PO_4)_3$ phase.[54] However, the position of the peaks in NVP kept unchanged, implying the stable structure of NVP. These results were further demonstrated by the *ex situ* XRD patterns (Fig. S15, ESI†). During the charging process, the diffraction peak of NTO was gradually shifted from 9.7° to 9.3°,

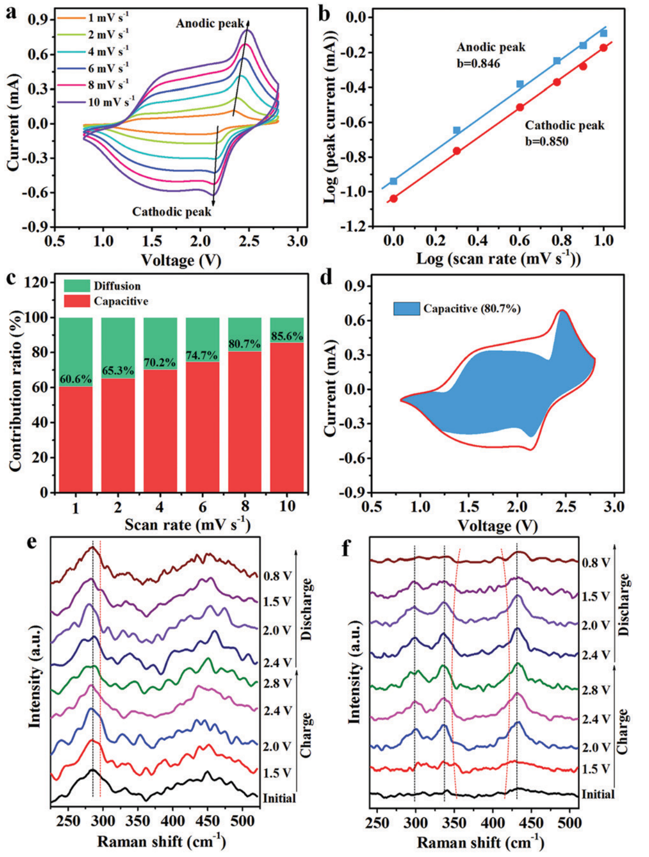

Fig. 3 Na-ion storage mechanism of NTO|NaBF$_4$-IE|NVP. (a) CV curves tested from 1 to 10 mV s^{-1}. (b) Current response *vs.* scan rate at the anodic and cathodic peaks. (c) Normalized capacitive ratio of the pseudocapacitive and diffusion-controlled contribution at different scan rates. (d) Total current (red) and capacitive current (blue) of NTO|NaBF$_4$-IE|NVP at 8 mV s^{-1}. (e and f) *In situ* Raman spectra of the NTO anode (e) and NVP cathode (f) in a full cell of NTO|NaBF$_4$-IE|NVP.

corresponding to a small expanded *d*-spacing from 0.90 nm to 0.95 nm, resulting from the Na$^+$ ion intercalation. Accordingly, the peak of NVP at 14.6° increased to 14.8° due to the desodiation process for the appearance of the Na$_1$V$_2$(PO$_4$)$_3$ phase, while the *d*-spacing of 0.60 nm imperceptibly decreased to 0.59 nm. It was observed that the Na-rich Na$_3$V$_2$(PO$_4$)$_3$ phase was eventually converted into the Na-poor Na$_1$V$_2$(PO$_4$)$_3$ phase at the end of this process,[55,56] indicative of two Na$^+$ ion transfers. During the discharging process, the characteristic peaks in the Raman spectra and XRD patterns well returned to the initial positions, demonstrative of the highly reversible (de)intercalation reaction for both NTO and NVP. It is emphasized that such reversible structural evolution with the small change of *d*-spacing during charging and discharging could guarantee the structural integrity of the anode and cathode films, which is highly favorable for improving long-term cyclability and flexibility. According to the above results and superiority of the planar geometry, we consider that planar microscale energy storage devices are an ideal model for the fundamental research of the charge storage mechanism using *in situ* characterization, where the structure evolution and morphology change of both the anode and cathode can be simultaneously *in situ* studied in a full cell (Fig. S16, ESI†).

It is worth noting that for NIMBs with an in-plane geometry, the two side surfaces and the upper surface of the microelectrode fingers were fully exposed within the ionogel electrolyte, which would greatly accelerate Na$^+$ ion transfer from these three surfaces or directions, thus resulting in enhanced performance. To demonstrate this uniqueness and importance of in-plane microelectrodes, a thin and tight EG layer was controllably deposited on the upper surface of NTO anode or NVP cathode fingers, respectively, and the corresponding microdevices were denoted as NTO|NaBF$_4$-IE|NVP-CN (EG cover on negative microelectrode) or NTO|NaBF$_4$-IE|NVP-CP (EG cover on positive microelectrode) (Fig. 4a and b) (see details in Methods). From SEM images (Fig. 4c–f), the NTO anode without an EG cover layer exposed substantial NTO particles on the upper surface and abundant porous channels (Fig. 4c), which was conducive to the infiltration of the ionogel electrolyte. In sharp contrast, with a compact smooth EG cover, the open channels and NTO active materials in NTO|NaBF$_4$-IE|NVP-CN were almost completely shielded (Fig. 4d). Likewise, the same phenomenon was observed in the NVP cathode of NTO|NaBF$_4$-IE|NVP and NTO|NaBF$_4$-IE|NVP-CP (Fig. 4e and f). Furthermore, the electrochemical performances of NTO|NaBF$_4$-IE|NVP, NTO|NaBF$_4$-IE|NVP-CN and NTO|NaBF$_4$-IE|NVP-CP are compared in Fig. 4g–i. Apparently, with the presence of the EG cover, the volumetric capacity and rate capability of both NTO|NaBF$_4$-IE|NVP-CN and NTO|NaBF$_4$-IE|NVP-CP visibly decreased (Fig. 4g), especially at high current densities. For instance, the volumetric capacity of NTO|NaBF$_4$-IE|NVP obtained at 10C was 21.9 mA h cm^{-3}, which was much higher than those of NTO|NaBF$_4$-IE|NVP-CN (17.5 mA h cm^{-3}) and NTO|NaBF$_4$-IE|NVP-CP (12.0 mA h cm^{-3}), accounting for the blocking effect of the tight EG cover layer that partly inhibited Na$^+$ ion transfer from the upper surface of the anode or cathode fingers. More interestingly, NTO|NaBF$_4$-IE|NVP presented a lower polarization voltage difference of 0.25 V in comparison with NTO|NaBF$_4$-IE|NVP-CN (0.34 V) and NTO|NaBF$_4$-IE|NVP-CP (0.37 V) (Fig. 4h). This result could be further explained by the smaller charge transfer resistance of 47 Ω for NTO|NaBF$_4$-IE|NVP than those of NTO|NaBF$_4$-IE|NVP-CN (81 Ω) and NTO|NaBF$_4$-IE|NVP-CP (85 Ω) (Fig. 4i and Fig. S17, ESI†), further proving that Na$^+$ ion diffusion would be blocked by the upper EG cover layer on the anodic or cathodic microelectrode. As shown in the above results, planar NTO|NaBF$_4$-IE|NVP possesses multi-directional Na$^+$ ion diffusion pathways from the two side surfaces and upper surface of the microelectrodes. It is noted that, at low current densities of 1C and 2C, the decrease of volumetric capacity of NTO|NaBF$_4$-IE|NVP-CP was less than those of NTO|NaBF$_4$-IE|NVP-CN, and *vice versa* at high current densities from 10C to 30C. This was possibly attributed to the different amount and diffusion rate of Na$^+$ ions from the varying surfaces of the microelectrode. According to the aforementioned results, there are multi-directional diffusion pathways for Na$^+$ ions in NTO|NaBF$_4$-IE|NVP. Specifically, if only considering two microelectrode fingers in the in-plane geometry, there should be four directions

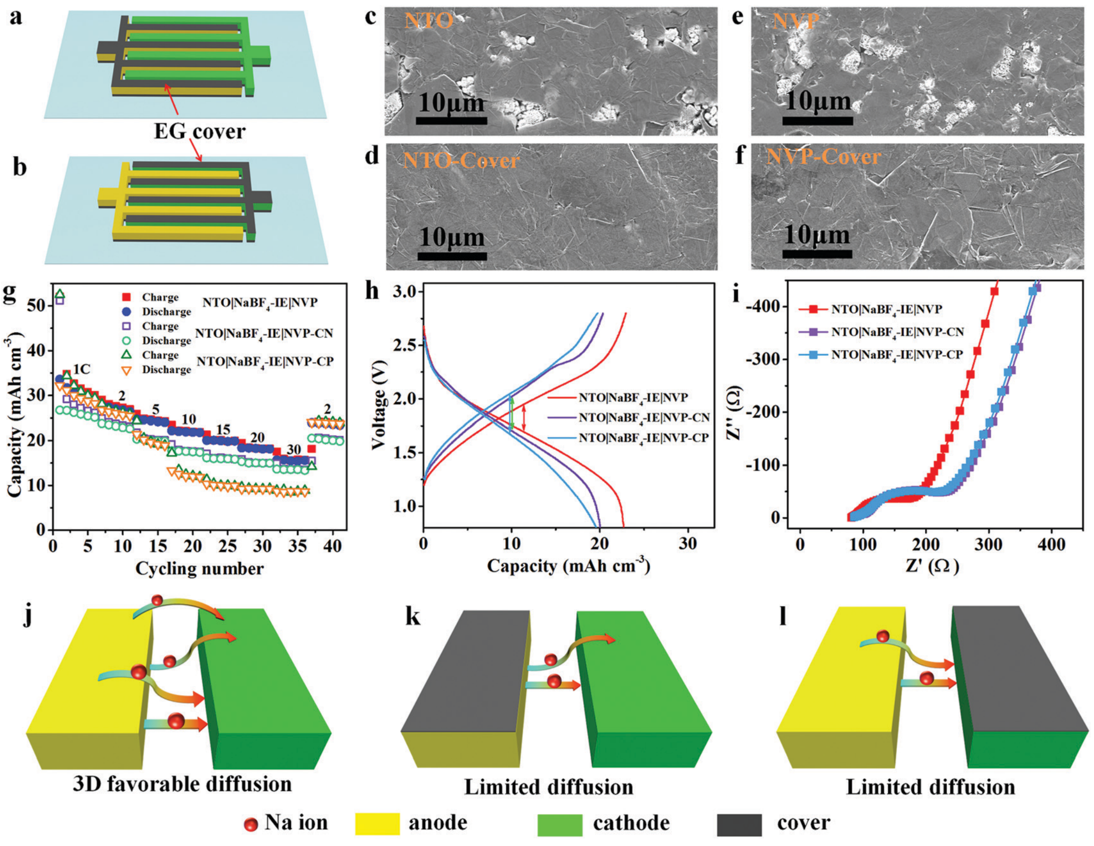

Fig. 4 3D multi-directional Na^+ ion diffusion mechanism of $NTO|NaBF_4$-IE|NVP. (a and b) Schematic diagram showing $NTO|NaBF_4$-IE|NVP with EG covering the NTO anodic microelectrode (a) and NVP cathodic microelectrode (b). (c and d) Top-view SEM images of the anodic microelectrode without (c) and with (d) the EG cover. (e and f) Top-view SEM images of the cathodic microelectrode without (e) and with (f) the EG cover. (g–i) Rate performance (g), GCD curves (h) and EIS spectra (i) of $NTO|NaBF_4$-IE|NVP, $NTO|NaBF_4$-IE|NVP-CN and $NTO|NaBF_4$-IE|NVP-CP. (j–l) Schematic illustration of 3D Na^+ ion transfer during the discharge process, showing that the cover can inhibit Na^+ ion transport in the vertical direction, suggestive of a multi-directional Na^+ ion diffusion mechanism of the NIMBs.

(Fig. 4j): two from the side surface of one microelectrode to the side and upper surfaces of the other microelectrode, and the other two from the upper surface to the side and upper surface. Once the anode or cathode part was closely coated with EG layer, Na^+ ion diffusion pathways are blocked to some extent in two directions, resulting in the capacity and rate performance decrease (Fig. 4k and l). In fact, planar $NTO|NaBF_4$-IE|NVP generally consists of several to tens of microelectrode fingers, therefore, the pathways of ion diffusion could be moved from the anode (cathode) fingers to the nearest adjacent cathode (anode) fingers or to the second adjacent cathode (anode) fingers or the far ones, exhibiting a 3D multi-directional ion diffusion mechanism to achieve high capacity and rate performance.

To satisfy the pursuit for flexible microelectronics, the electrochemical performance of quasi-solid-state planar $NTO|NaBF_4$-IE|NVP was evaluated at various bending states from 0° to circling state (>180°, Fig. 5a and b). It was observed that the shapes of the GCD profiles at 10C almost overlapped, and the capacity remained unchanged with coulombic efficiency of 100% under various bending states (Fig. 5a and Fig. S18a, ESI†), indicative of excellent mechanical flexibility of $NTO|NaBF_4$-IE|NVP. When the microdevices were repeatedly bent 1000 times, the capacity of $NTO|NaBF_4$-IE|NVP exhibited only a slight fluctuation with 100% coulombic efficiency (Fig. S18b, ESI†). It should be emphasized that, during the flexibility testing process, there was no breakage of the microelectrodes or separation between the microelectrodes and substrate, implying the excellent structural and electrochemical stability of $NTO|NaBF_4$-IE|NVP. Moreover, our $NTO|NaBF_4$-IE|NVP was ready to be integrated in series or in parallel through one by one filtration and simply overlapping the ends of the microelectrodes for the interconnection of two adjacent microdevices (Fig. 1j–l). Importantly, the integrated $NTO|NaBF_4$-IE|NVP connected in series or in parallel showed similar shapes of the GCD curves, suggesting the same electrochemical behaviors. The serially connected $NTO|NaBF_4$-IE|NVP monotonously increased the plateau voltage with discharge time unchanged (Fig. 5c), and the parallelly connected $NTO|NaBF_4$-IE|NVP showed a stable average plateau voltage with proportional increase of the discharge time (Fig. S19, ESI†), demonstrating consistent and outstanding performance. Moreover, three serially-connected $NTO|NaBF_4$-IE|NVP could easily light "DICP" letters consisting of 42 light emitting diodes (LEDs) in severe convex and concave deformation (Fig. 5d), holding great potential to be

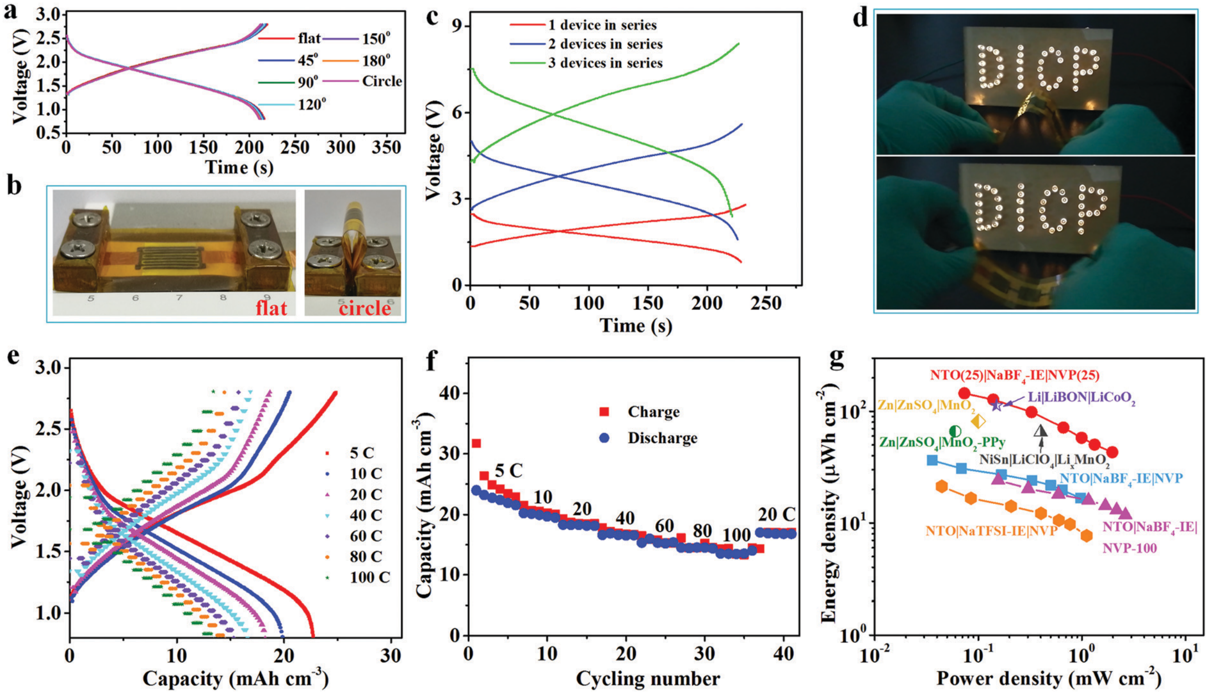

Fig. 5 Flexibility and high-temperature performance of NTO|NaBF$_4$-IE|NVP. (a) GCD curves obtained at different bending states. (b) Photographs of NTO|NaBF$_4$-IE|NVP in flat and circling states. (c) GCD profiles of serial NTO|NaBF$_4$-IE|NVP with one, two and three cells. (d) Optical images of the letters "DICP" composed of 42 LEDs powered by three tandem NTO|NaBF$_4$-IE|NVP under different bending states. (e) GCD curves, and (f) rate performance obtained at current densities from 5 to 100C at 100 °C. (g) Ragone plot of NIMBs compared with the previously reported micro-batteries.

applied as efficient micropower sources for flexible electronic devices.

Because of the usage of flammable and volatile organic electrolyte, conventional organic electrolyte based batteries usually suffer from serious safety issues at increased temperatures (>60 °C).[57–59] Here, our quasi-solid-state NIMBs demonstrated high thermal stability within a wide range of operating temperatures (25–100 °C). The electrochemical performance of NTO|NaBF$_4$-IE|NVP was investigated at the high temperature of 100 °C (denoted as NTO|NaBF$_4$-IE|NVP-100), considering the NaBF$_4$-IE can be stable up to 300 °C (Fig. S20, ESI†) and nonflammability in comparison with the commercial sodium ion gel electrolyte (Fig. S21, ESI†). As shown in Fig. 5e, the GCD curves of NTO|NaBF$_4$-IE|NVP-100 measured at various rates exhibited similar electrochemical behavior to NTO|NaBF$_4$-IE|NVP at room temperature. Surprisingly, NTO|NaBF$_4$-IE|NVP-100 could be ultrafast discharged and charged at an ultrahigh rate of 100C within an extremely short time of 15–20 s, delivering a significant capacity of 13.5 mA h cm^{-3} (Fig. 5f), corresponding to 57.9% of the initial capacity at 5C. The low coulombic efficiency at high temperature of 100 °C was ascribed to the side effects, such as oxygen emission and metal dissolution of NTO and NVP.[57,58] Such exceptional rate performance mainly resulted from the remarkably decreased charge transfer resistance (63 Ω, Fig. S22, ESI†), owing to the greatly improved ionic conductivity of NaBF$_4$-IE from 8.1 mS cm^{-1} at 25 °C to 25 mS cm^{-1} at 100 °C. In addition, NTO|NaBF$_4$-IE|NVP-100 still maintained a high volumetric capacity of 10.1 mA h cm^{-3} after 400 cycles at 60C (Fig. S23, ESI†), indicating high temperature stability.

A Ragone plot compared the areal/volumetric energy density and power density in volume of NTO|NaBF$_4$-IE|NVP, NTO|NaBF$_4$-IE|NVP-100, NTO|NaTFSI-IE|NVP and previous micro-scale energy storage devices (Fig. 5g and Fig. S24, ESI†). NTO(25)|NaBF$_4$-IE|NVP(25) displayed high areal energy density of 145 μW h cm^{-2}, which was much higher than those reported for lithium/zinc ion MBs, such as Li|LiBON|LiCoO$_2$ (113 μW h cm^{-2}),[60] NiSn|LiClO$_4$|Li$_x$MnO$_2$ (65 μW h cm^{-2}),[16] Zn|ZnSO$_4$|MnO$_2$ (81.5 μW h cm^{-2}),[61] and Zn|ZnSO$_4$|MnO$_2$-PPy (66 μW h cm^{-2}).[62] It was also observed that NTO(25)|NaBF$_4$-IE|NVP(25) displayed a high areal power density of 1.9 mW cm^{-2}, which was higher than those lithium and Zn ion MBs reported (0.1–1 mW cm^{-2}). Notably, it was revealed that NTO|NaBF$_4$-IE|NVP delivered a volumetric energy density of 55.6 mW h cm^{-3} (Fig. S24, ESI†), which was higher than those of NTO|NaBF$_4$-IE|NVP-CN (47.2 mW h cm^{-3}), NTO|NaBF$_4$-IE|NVP-CP (54.5 mW h cm^{-3}), and NTO|NaTFSI-IE|NVP (32.6 mW h cm^{-3}), and is well comparable with most of the reported MBs, for instance, carbon|LiClO$_4$|polypyrrole (PPy, 20 mW h cm^{-3}),[63] Li|LiBON|LiCoO$_2$ (83 mW h cm^{-3})[60] NiSn|LiClO$_4$|Li$_x$MnO$_2$ (65 mW h cm^{-3}),[16] and Zn|ZnSO$_4$|MnO$_2$ micro-batteries (17.9 mW h cm^{-3}).[64] Moreover, our NTO|NaBF$_4$-IE|NVP at room temperature delivered a power density of 1.5 W cm^{-3} and the volumetric power density of NTO|NaBF$_4$-IE|NVP-100 increased to 4.0 W cm^{-3}, higher than those of the micro-batteries previously reported.[60–62]

Conclusions

In summary, we have demonstrated the fabrication of quasi-solid-state planar ionogel-based NIMBs with interdigital micro-patterns of an urchin-like NTO anode and a flower-like NVP cathode, where EG as a 2D additive, soft support and metal-free current collector endowed the fabricated microelectrodes with a stable structure, high electrical conductivity and excellent flexibility. Through the combined benefits from the highly ionically conductive $NaBF_4$-based ionogel electrolyte and dominant pseudocapacitance contribution, the as-assembled NTO|$NaBF_4$-IE|NVP showed high volumetric capacity, enhanced rate capability, high-temperature stability up to 100 °C, and ultra-high areal energy density of 145 μW h cm^{-2} (55.6 mW h cm^{-3}). Moreover, NTO|$NaBF_4$-IE|NVP revealed 3D multi-directional pathways for sodium ion diffusion, which can provide a universal guidance to improve the performance of other planar micro-batteries. Planar miniaturized energy storage devices are an ideal model to use *in situ* characterization for fundamental research on the charge storage mechanism. This study shows that by fully utilizing a multi-directional ion diffusion mechanism and reasonably designing the conducting compact micro-electrodes, the energy density and power density of NIMBs or other micro-batteries can be further improved simultaneously, holding tremendous potential for many pervasive applications in microelectronics and microsystems.

Conflicts of interest

There are no conflicts to declare.

Acknowledgements

This work was financially supported by the National Key R@D Program of China (Grant 2016YBF0100100), the National Natural Science Foundation of China (Grant No. 51872283, 21805273, 51925207, U1910210 and 51872277), Dalian National Laboratory For Clean Energy (DNL), CAS, DNL Cooperation Fund, CAS (DNL180310, DNL180308, DNL201912, and DNL201915), Liao Ning Revitalization Talents Program (Grant XLYC1807153), the Natural Science Foundation of Liaoning Province, Joint Research Fund Liaoning-Shenyang National Laboratory for Materials Science (Grant 20180510038), DICP (DICP ZZBS201708, DICP ZZBS201802), and DICP&QIBEBT (Grant DICP&QIBEBT UN201702), and the Fundamental Research Funds for the Central Universities (WK2060140026).

References

1 M. Beidaghi and Y. Gogotsi, *Energy Environ. Sci.*, 2014, **7**, 867–884.
2 P. Zhang, F. Wang, M. Yu, X. Zhuang and X. Feng, *Chem. Soc. Rev.*, 2018, **47**, 7426–7451.
3 P. Huang, C. Lethien, S. Pinaud, K. Brousse, R. Laloo, V. Turq, M. Respaud, A. Demortière, B. Daffos, P. L. Taberna, B. Chaudret, Y. Gogotsi and P. Simon, *Science*, 2016, **351**, 691–695.
4 A. Sumboja, J. Liu, W. G. Zheng, Y. Zong, H. Zhang and Z. Liu, *Chem. Soc. Rev.*, 2018, **47**, 5919–5945.
5 D. Qi, Y. Liu, Z. Liu, L. Zhang and X. Chen, *Adv. Mater.*, 2017, **29**, 1602802.
6 C. Lethien, J. Le Bideau and T. Brousse, *Energy Environ. Sci.*, 2019, **12**, 96–115.
7 H. Nishide and K. Oyaizu, *Science*, 2008, **319**, 737–738.
8 C. Liu, E. I. Gillette, X. Chen, A. J. Pearse, A. C. Kozen, M. A. Schroeder, K. E. Gregorczyk, S. B. Lee and G. W. Rubloff, *Nat. Nanotechnol.*, 2014, **9**, 1031.
9 J. F. M. Oudenhoven, L. Baggetto and P. H. L. Notten, *Adv. Energy Mater.*, 2011, **1**, 10–33.
10 N. Kamboj, T. Purkait, M. Das, S. Sarkar, K. S. Hazra and R. S. Dey, *Energy Environ. Sci.*, 2019, **12**, 2507–2517.
11 S. Zheng, Z.-S. Wu, F. Zhou, X. Wang, J. Ma, C. Liu, Y.-B. He and X. Bao, *Nano Energy*, 2018, **51**, 613–620.
12 J. I. Hur, L. C. Smith and B. Dunn, *Joule*, 2018, **2**, 1187–1201.
13 L. X. Liu, Q. H. Weng, X. Y. Lu, X. L. Sun, L. Zhang and O. G. Schmidt, *Small*, 2017, **13**, 1701847.
14 S. Ferrari, M. Loveridge, S. D. Beattie, M. Jahn, R. J. Dashwood and R. Bhagat, *J. Power Sources*, 2015, **286**, 25–46.
15 B. L. Ellis, P. Knauth and T. Djenizian, *Adv. Mater.*, 2014, **26**, 3368–3397.
16 H. L. Ning, J. H. Pikul, R. Y. Zhang, X. J. Li, S. Xu, J. J. Wang, J. A. Rogers, W. P. King and P. V. Braun, *Proc. Natl. Acad. Sci. U. S. A.*, 2015, **112**, 6573–6578.
17 S. Zheng, X. Shi, P. Das, Z.-S. Wu and X. Bao, *Adv. Mater.*, 2019, **0**, 1900583.
18 J.-Q. Xie, Y.-Q. Ji, J.-H. Kang, J.-L. Sheng, D.-S. Mao, X.-Z. Fu, R. Sun and C.-P. Wong, *Energy Environ. Sci.*, 2019, **12**, 194–205.
19 J. F. Ni and L. Li, *Adv. Funct. Mater.*, 2018, **28**, 1704880.
20 N. Yabuuchi, K. Kubota, M. Dahbi and S. Komaba, *Chem. Rev.*, 2014, **114**, 11636–11682.
21 C. Zhao, C. Yu, B. Qiu, S. Zhou, M. Zhang, H. Huang, B. Wang, J. Zhao, X. Sun and J. Qiu, *Adv. Mater.*, 2018, **30**, 1702486.
22 N. Wang, C. Chu, X. Xu, Y. Du, J. Yang, Z. Bai and S. Dou, *Adv. Energy Mater.*, 2018, **8**, 1801888.
23 Q. Lin, J. Zhang, D. Kong, T. Cao, S.-W. Zhang, X. Chen, Y. Tao, W. Lv, F. Kang and Q.-H. Yang, *Adv. Energy Mater.*, 2018, **9**, 1803078.
24 M. Lee, J. Hong, J. Lopez, Y. M. Sun, D. W. Feng, K. Lim, W. C. Chueh, M. F. Toney, Y. Cui and Z. N. Bao, *Nat. Energy*, 2017, **2**, 861–868.
25 J. Y. Hwang, S. T. Myung and Y. K. Sun, *Chem. Soc. Rev.*, 2017, **46**, 3529–3614.
26 A. Ponrouch, D. Monti, A. Boschin, B. Steen, P. Johansson and M. R. Palacín, *J. Mater. Chem. A*, 2015, **3**, 22–42.
27 Y. Lu, L. Li, Q. Zhang, Z. Niu and J. Chen, *Joule*, 2018, **2**, 1747–1770.
28 Y. Sun, P. C. Shi, H. F. Xiang, X. Liang and Y. Yu, *Small*, 2019, **15**, 1805479.
29 S. Fu, J. Ni, Y. Xu, Q. Zhang and L. Li, *Nano Lett.*, 2016, **16**, 4544–4551.

30 J. Ni, S. Fu, C. Wu, Y. Zhao, J. Maier, Y. Yu and L. Li, *Adv. Energy Mater.*, 2016, **6**, 1502568.

31 L. Liang, Y. Xu, C. Wang, L. Wen, Y. Fang, Y. Mi, M. Zhou, H. Zhao and Y. Lei, *Energy Environ. Sci.*, 2015, **8**, 2954–2962.

32 M. Fan, Y. Chen, Y. Xie, T. Yang, X. Shen, N. Xu, H. Yu and C. Yan, *Adv. Funct. Mater.*, 2016, **26**, 5019–5027.

33 D. Chao, C. Zhu, P. Yang, X. Xia, J. Liu, J. Wang, X. Fan, S. V. Savilov, J. Lin, H. J. Fan and Z. X. Shen, *Nat. Commun.*, 2016, **7**, 12122.

34 D. Xie, X. Xia, Y. Zhong, Y. Wang, D. Wang, X. Wang and J. Tu, *Adv. Energy Mater.*, 2017, **7**, 1601804.

35 Y. L. Zhong and T. M. Swager, *J. Am. Chem. Soc.*, 2012, **134**, 17896–17899.

36 F. Zhou, H. Huang, C. Xiao, S. Zheng, X. Shi, J. Qin, Q. Fu, X. Bao, X. Feng, K. Müllen and Z.-S. Wu, *J. Am. Chem. Soc.*, 2018, **140**, 8198–8205.

37 Y. Dong, Z.-S. Wu, S. Zheng, X. Wang, J. Qin, S. Wang, X. Shi and X. Bao, *ACS Nano*, 2017, **11**, 4792–4800.

38 Y. Liu, C. Yang, Q. Zhang and M. Liu, *Energy Storage Mater.*, 2019, **22**, 66.

39 Y. Jiang, X. Zhou, D. Li, X. Cheng, F. Liu and Y. Yu, *Adv. Energy Mater.*, 2018, **8**, 1800068.

40 S. Li, Y. Dong, L. Xu, X. Xu, L. He and L. Mai, *Adv. Mater.*, 2014, **26**, 3545–3553.

41 X. Rui, W. Sun, C. Wu, Y. Yu and Q. Yan, *Adv. Mater.*, 2015, **27**, 6670–6676.

42 C. Ding, T. Nohira, K. Kuroda, R. Hagiwara, A. Fukunaga, S. Sakai, K. Nitta and S. Inazawa, *J. Power Sources*, 2013, **238**, 296–300.

43 J. Evans, C. A. Vincent and P. G. Bruce, *Polymer*, 1987, **28**, 2324–2328.

44 T. Dong, J. Zhang, G. Xu, J. Chai, H. Du, L. Wang, H. Wen, X. Zang, A. Du, Q. Jia, X. Zhou and G. Cui, *Energy Environ. Sci.*, 2018, **11**, 1197–1203.

45 D. Xu, J. Su, J. Jin, C. Sun, Y. Ruan, C. Chen and Z. Wen, *Adv. Energy Mater.*, 2019, **9**, 1900611.

46 D. Xu, J. Jin, C. Chen and Z. Wen, *ACS Appl. Mater. Interfaces*, 2018, **10**, 38526–38537.

47 W. Liu, S. W. Lee, D. Lin, F. Shi, S. Wang, A. D. Sendek and Y. Cui, *Nat. Energy*, 2017, **2**, 17035.

48 J. Wang, J. Polleux, J. Lim and B. Dunn, *J. Phys. Chem. C*, 2007, **111**, 14925–14931.

49 V. Augustyn, J. Come, M. A. Lowe, J. W. Kim, P.-L. Taberna, S. H. Tolbert, H. D. Abruña, P. Simon and B. Dunn, *Nat. Mater.*, 2013, **12**, 518.

50 T. Kasuga, M. Hiramatsu, A. Hoson, T. Sekino and K. Niihara, *Adv. Mater.*, 1999, **11**, 1307–1311.

51 Y. Zhang, L. Guo and S. Yang, *Chem. Commun.*, 2014, **50**, 14029–14032.

52 X.-d. Meng, D.-z. Wang, J.-h. Liu and S.-y. Zhang, *Mater. Res. Bull.*, 2004, **39**, 2163–2170.

53 N. Membreño, P. Xiao, K.-S. Park, J. B. Goodenough, G. Henkelman and K. J. Stevenson, *J. Phys. Chem. C*, 2013, **117**, 11994–12002.

54 C. Kim, N. S. Norberg, C. T. Alexander, R. Kostecki and J. Cabana, *Adv. Funct. Mater.*, 2013, **23**, 1214–1222.

55 G. Li, Z. Yang, Y. Jiang, C. Jin, W. Huang, X. Ding and Y. Huang, *Nano Energy*, 2016, **25**, 211–217.

56 W. Ren, Z. Zheng, C. Xu, C. Niu, Q. Wei, Q. An, K. Zhao, M. Yan, M. Qin and L. Mai, *Nano Energy*, 2016, **25**, 145–153.

57 M.-T. F. Rodrigues, K. Kalaga, H. Gullapalli, G. Babu, A. L. M. Reddy and P. M. Ajayan, *Adv. Energy Mater.*, 2016, **6**, 1600218.

58 M. T. F. Rodrigues, G. Babu, H. Gullapalli, K. Kalaga, F. N. Sayed, K. Kato, J. Joyner and P. M. Ajayan, *Nat. Energy*, 2017, **2**, 17108.

59 Y. Qiao, Y. He, K. Jiang, Y. Liu, X. Li, M. Jia, S. Guo and H. Zhou, *Adv. Energy Mater.*, 2018, **8**, 1802322.

60 S. W. Song, K. C. Lee and H. Y. Park, *J. Power Sources*, 2016, **328**, 311–317.

61 G. Q. Sun, X. T. Jin, H. S. Yang, J. Gao and L. T. Qu, *J. Mater. Chem. A*, 2018, **6**, 10926–10931.

62 M. Zhu, Z. Wang, H. Li, Y. Xiong, Z. Liu, Z. Tang, Y. Huang, A. L. Rogach and C. Zhi, *Energy Environ. Sci.*, 2018, **11**, 2414–2422.

63 H.-S. Min, B. Y. Park, L. Taherabadi, C. Wang, Y. Yeh, R. Zaouk, M. J. Madou and B. Dunn, *J. Power Sources*, 2008, **178**, 795–800.

64 X. Wang, S. Zheng, F. Zhou, J. Qin, X. Shi, S. Wang, C. Sun, X. Bao and Z.-S. Wu, *Natl. Sci. Rev.*, 2019, DOI: 10.1093/nsr/nwz070.